Leaky-dielectric phase field model for the axisymmetric breakup of an electrified jet

Kaartikey Misra and Manuel Gamero-Castaño *
Department of Mechanical and Aerospace Engineering, University of California, Irvine, California 92697, USA

(Received 6 February 2022; accepted 24 May 2022; published 9 June 2022)

This article develops a leaky-dielectric model to study the axisymmetric breakup of an electrified jet, using the phase field method to treat interfacial phenomena. The model is used to analyze the breakup in a wide range of the Taylor number (Γ), the Ohnesorge number (Oh), and the wave number relevant to electrosprays operating in the cone-jet mode. The phase field technique accurately captures the behavior of the jet after pinch-off and predicts the formation of primary and satellite droplets. The numerical results are compared with existing experimental and numerical studies, extending them to account for the formation of sub-satellite droplets. It is found that for highly viscous jets, Oh $\gg$ 1, the number of subsatellite droplets generated increases with the Taylor number when compared to low viscous jets, hence widening the size distribution of droplets. At fixed Γ and Oh the primary droplets are charged to an approximately constant ratio of the Rayleigh charge limit, regardless of the wave number. Furthermore, the primary droplets are charged below the Rayleigh limit for $\Gamma \lesssim 1.5$ and charged above the Rayleigh limit when $\Gamma \gtrsim 1.5$. Thus, most primary droplets are expected to be unstable at Taylor numbers exceeding 1.5.

DOI: 10.1103/PhysRevFluids.7.064004

I. INTRODUCTION

Electrosprays operating in the cone-jet mode [1,2] are characterized by the emission of a stationary and long jet from the vertex of a liquid meniscus, resulting from the interplay between an imposed electric field, the fluid dynamics of the liquid, and its surface tension. The natural instability of the jet is suppressed by the accelerating effect of the electric field, but once the latter becomes sufficiently weak away from the vertex, the jet becomes unstable and breaks into charged droplets [3,4]. The axisymmetric breakup of the stationary jet produces droplets characterized by a narrow distribution of diameters with an average that depends on the physical properties of the liquid and its flow rate. Various technological applications benefit from such fine sprays [5,6], making the study of the breakup not only of fundamental but also of practical interest. The problem of destabilization and breakup of electrified jets is usually studied either using linear stability analysis (small deformation), or a nonlinear numerical approach (large deformation).

Linear stability analyses consider an infinitely long cylindrical jet of radius R_j, and impose a sinusoidal perturbation on the surface so that its position can be defined as $R = R_j(1 + \epsilon e^{st+ikz/R_j})$, where s is the growth rate of the perturbation, k its specified wave number, and ϵ an arbitrarily small number. An arbitrary perturbation can be expressed as an infinite series of these k-normal modes and, since the system is linear, the response can be computed with the individual solutions for each normal mode. The basic goal of the analysis is to find the range of wave numbers for which the growth rate is positive, i.e., which make the jet unstable. Furthermore the wave number with

*mgameroc@uci.edu

fastest growth rate yields the diameter of the droplet most likely to be produced by the breakup, or modal droplet. Basset [7] analyzed the breakup of an equipotential and inviscid jet subjected to axisymmetric perturbations. Melcher [8] extended Basset's analysis by including both axisymmetric and nonaxisymmetric perturbations. Saville [9] included viscosity into the equipotential problem, and found that when the viscosity is sufficiently high, the axisymmetric instability modes are damped and nonaxisymmetric modes dominate, leading to jet whipping [9,10]. Mestel [11,12] relaxed the assumption of equipotential breakup and investigated the effect of surface charge and tangential electrical stresses. López-Herrera *et al.* [13] used linear stability analysis to study the deformation and breakup of jets with finite electrical conductivity, and the role of a downstream electrode. Wang [14] studied the breakup of jets with finite electrical conductivity using both linear stability and nonlinear analysis for jets surrounded by another viscous medium in the Stokes limit.

Linear stability analysis can only probe the initial stages of the breakup, and the study of phenomena dependent on large deformation such as the generation of satellite droplets requires the use of nonlinear numerical calculations. Setiawan and Heister [15] formulated a nonlinear boundary element algorithm (BEM) to study the axisymmetric breakup of an inviscid and equipotential jet. They considered high electrification levels and observed the formation of satellite droplets along with primary droplets. They calculated pinch-off times and the sizes of primary and satellite droplets. López-Herrera *et al.* [16] extended the model of Lee [17] to study the breakup of a viscous and equipotential jet at low electrification levels and low-moderate viscosities. They calculated the sizes and charges of the primary and satellite droplets for different wave numbers. The numerical results were found to be in good agreement with experimental data [18]. Collins *et al.* [19] studied the equipotential breakup of a jet subjected to a radial electric field, for wide ranges of electrification and viscosity levels. They showed that as the level of electrification increases, the size of the satellite droplet increases monotonically, thereby reducing the size of primary droplets. They also showed that for a fixed electrification level, the size of satellite droplets decreases as the viscosity increases, a trend also observed in the experiments of López-Herrera and Gañán-Calvo [18]. For high electrification, the charges carried by primary and satellite droplets can exceed the Rayleigh [20] stability limit, leading to the possibility of the subsequent breakup of these droplets. Collins *et al.* [19] also showed that satellite droplets are produced for electrified jet's in the Stoke's limit. This feature is not observed in uncharged jets, but has been reported when the jet is surrounded by a viscous medium [21,22]. Wang and Papageorgiou [23] studied the nonlinear breakup of a perfect conducting viscous thread surrounded by another viscous medium at zero Reynolds number. Nie *et al.* [24] developed a leaky-dielectric electrohydrodynamic (EHD) model to study the role of different charge relaxation mechanisms on the pinch-off and formation of satellite droplets. A distinction must be made between the implementation of the equipotential condition by several authors. It is always possible to impose a constant potential on the surface of the jet, e.g., as in Ref. [19]. In this case the potential field inside the jet is constant and does not need to be resolved, but the total charge in the simulated section of the jet is not conserved. However, one can ensure quasiequipotentiality by including a conservation of charge equation in the model, imposing an electric relaxation time much smaller than the breakup time, and solving for the potential inside the jet. This approach ensures conservation of charge and therefore is more physical. López-Herrera and Gañán-Calvo [18] and Li *et al.* [25] discuss in detail these two approaches.

Few nonlinear models utilize the volume of fluid or the level set methods to study the deformation and breakup of electrified jets. These phase field methods are useful to reproduce the formation of additional subsatellite droplets after the first pinch-off. Eck *et al.* [26] developed a phase field model for electrowetting. They coupled the Navier-Stokes equation and electrostatic charge transport equations with the Cahn-Hilliard phase field equations. For the EHD system in two and three dimensions, they proved the existence of weak solutions for the governing dynamics of electrowetting. Lakdawala *et al.* [27] formulated a dual grid level set method to study the breakup of conducting liquid threads of low viscosity and electrification level. They showed that, for sufficiently long perturbations, subsatellite droplets may also form along with the primary and satellite droplets. López-Herrera *et al.* [28] developed a volume of fluid model to study the role of electrokinetic

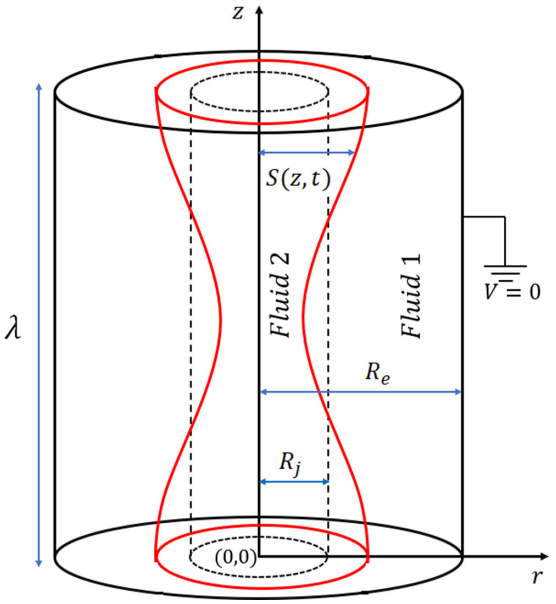

FIG. 1. Schematic of the problem and computational domain.

effects on the deformation and breakup of conducting jets when the breakup time is comparable or smaller than the diffusion timescale.

Existing nonlinear analyses do not capture the liquid threads formed after pinch-off and which may generate subsatellite droplets [19,23,29,30]. Moreover, most existing nonlinear analysis have imposed the constant-potential condition and usually study jets under low or moderate levels of electrification. Motivated by this, the present article develops a phase field, leaky-dielectric EHD model to study the axisymmetric breakup of an electrified jet. The model does not consider the effect of an imposed axial electric field, which is negligible in the breakup region of most cone-jets [16,18,31,32], and is not applicable to sinuous or whipping instabilities and ramified jet breakups [5,33]. The remainder of the article is organized as follows: Section II presents the description of the model along with the numerical procedure. Section III establishes the connection between the sets of dimensionless numbers parametrizing the breakup and cone-jets. In Sec. IV the numerical solution is validated with existing experimental and numerical results (Sec. IV A), and the breakup is investigated for selected wave numbers and broad ranges of the Ohnesorge and Taylor numbers (Secs. IV B and IV C). Concluding remarks are presented in Sec. V.

II. PROBLEM FORMULATION AND NUMERICAL SETUP

For the numerical calculations we assume an infinitely long jet subjected to a small periodic perturbation with a given wave number, and we follow the evolution of a section of the jet using periodic boundary conditions. This framework follows the linear analysis technique and is commonly used to study the nonlinear, long deformation problem (for reference see López-Herrera *et al.* [13,16], López-Herrera and Gañán-Calvo [18], Collins *et al.* [19], Nie *et al.* [24], Lakdawala *et al.* [27], López-Herrera *et al.* [34]). Figure 1 depicts the schematic of the problem, modeled in cylindrical $\{z, r\}$ coordinates. The domain contains a liquid jet of length λ (Fluid 2), separated from a surrounding liquid (Fluid 1) by an interface $r = S(z, t)$. Fluid 1 is further enclosed by a cylindrical electrode of radius R_e. In its unperturbed state the jet has a radius R_j and a net charge q distributed

homogeneously on its surface, inducing a normal electric field E_{no},

$$E_{\text{no}} = \frac{q}{2\pi\varepsilon_0 R_j \lambda}. \tag{1}$$

To study the stability of the system a small sinusoidal perturbation is added to the position of the interface

$$S(z,0) = R_j\left(1 + A\cos\frac{kz}{R_j}\right), \quad k = \frac{2\pi R_j}{\lambda}. \tag{2}$$

In the numerical simulations we use $A = 0.015$ and $R_e = 12R_j$. The relevant physical properties of the fluids are the electrical conductivity K_i, relative permittivity ε_i, viscosity μ_i, and density ρ_i, as well as the surface tension γ of the interface. The subscript i indicates either Fluid 1 or 2.

The interface between the jet and the outer medium is modeled as a diffuse interface using the phase field method [35]. A continuous phase variable ϕ is defined throughout the domain, varying from -1 to 1 between the bulks of Fluids 1 and 2, respectively, and fulfilling the Cahn-Hilliard equation [35–37]. The phase variables changes rapidly across the narrow, yet finite, thickness of the diffuse interface, so that the surface where $\phi = 0$ defines the mean interface $S(z,t)$. The physical properties are defined as continuous functions of ϕ throughout the domain. In particular the density, the viscosity and the relative electrical permittivity are defined as the weighted arithmetic mean of ϕ, whereas, the electrical conductivity is defined as its weighted harmonic mean [38–40]:

$$\rho = \rho_1\left(\frac{1-\phi}{2}\right) + \rho_2\left(\frac{1+\phi}{2}\right), \quad \mu = \mu_1\left(\frac{1-\phi}{2}\right) + \mu_2\left(\frac{1+\phi}{2}\right), \tag{3}$$

$$\varepsilon = \varepsilon_1\left(\frac{1-\phi}{2}\right) + \varepsilon_2\left(\frac{1+\phi}{2}\right), \quad \frac{1}{K} = \frac{1}{K_1}\left(\frac{1-\phi}{2}\right) + \frac{1}{K_2}\left(\frac{1+\phi}{2}\right). \tag{4}$$

Fluid 1 consists of vacuum space, i.e., μ_1 and ρ_1 are zero while $\varepsilon_1 = 1$; we set its electrical conductivity to a very small value, $K_1 = 10^{-12} S/m$. The model solves for the velocity $\boldsymbol{u}$, pressure p, and volumetric charge ρ_e, the electric potential V (the electric field is simply $\boldsymbol{E} = -\nabla V$), and the phase field variable ϕ as functions of position and time. These field variables fulfill the equations of conservation of mass, momentum and charge, the Poisson equation, and the Cahn-Hilliard equation. They are written in dimensionless form using $l_c = R_j$, $t_c = \sqrt{\rho_2 R_j^3/\gamma}$, $v_c = l_c/t_c$, $p_c = \rho_2 v_c^2$, $E_c = E_{\text{no}}$, and $\rho_{e,c} = \varepsilon_0 E_{\text{no}}/R_j$ as the characteristic scales for length, time, velocity, pressure, electric field, and volumetric charge, respectively:

$$\nabla\cdot\boldsymbol{u} = 0, \tag{5}$$

$$\frac{\partial(\frac{\rho}{\rho_2}\boldsymbol{u})}{\partial t} + \nabla\cdot\left(\frac{\rho}{\rho_2}\boldsymbol{u}\boldsymbol{u}\right) = -\nabla p + \text{Oh}\nabla\cdot\frac{\mu}{\mu_2}(\nabla\boldsymbol{u} + \nabla\boldsymbol{u}^T) + \Gamma\boldsymbol{F}_{\text{es}} + \boldsymbol{F}_{\text{st}}, \tag{6}$$

$$\frac{\partial\rho_e}{\partial t} + \nabla\cdot(\rho_e\boldsymbol{u}) = \frac{1}{\Pi_t}\nabla\cdot\left(\frac{K}{K_2}\boldsymbol{E}\right), \tag{7}$$

$$\varepsilon\nabla^2 V + \nabla V\cdot\nabla\varepsilon = -\rho_e, \tag{8}$$

$$\frac{\partial\phi}{\partial t} + \boldsymbol{u}\cdot\nabla\phi = \frac{1}{\text{Pe}}\nabla^2\psi, \quad \psi = \frac{1}{\xi}(\phi^2-1)\phi - \xi\nabla^2\phi, \tag{9}$$

where $\boldsymbol{F}_{\text{es}}$ is the electric body force [41]

$$\boldsymbol{F}_{\text{es}} = \nabla\cdot\boldsymbol{T}_e = \nabla\cdot\varepsilon\left(\boldsymbol{E}\boldsymbol{E} - \tfrac{1}{2}\boldsymbol{I}|E|^2\right) = \rho_e\boldsymbol{E} - \tfrac{1}{2}\nabla\varepsilon\boldsymbol{E}\cdot\boldsymbol{E}, \tag{10}$$

and $\boldsymbol{F}_{\mathrm{st}}$ is the surface tension body force [36,37]

$$\boldsymbol{F}_{\mathrm{st}} = \psi \nabla \phi. \tag{11}$$

ξ in the Cahn-Hilliard equation (9) is the dimensionless interface thickness parameter, which provides a measure of the sharpness of the interface. In the sharp interface limit, the diffuse interface thickness goes to zero. In practice, the phase variable and the velocity are independent of the thickness parameter when the latter is sufficiently small, $\xi \lesssim 0.01$–0.03 [36]. Unlike the classical leaky-dielectric formulation of Saville [42], our model includes a conservation equation for the volumetric charge that retains convective and conduction terms, i.e., we do not require the electrical relaxation term to be much smaller than the characteristic time of the flow, and uses the volumetric charge as the source term in the Poisson equation for the electric potential. However, the model follows the leaky-dielectric convention of omitting electrokinetic effects, which are replaced by a physical property, namely, the electrical conductivity. The classical formulation of the leaky-dielectric model has been demonstrated to be accurate in the description of cone-jets [43], a problem similar to the present one.

Equations (5)–(11) include five dimensionless numbers: Oh, Γ, Π_t, Pe and the relative permittivity of the jet ε_2. The Ohnesorge number is the ratio between the viscous timescale $t_\mu = \mu_2 R_j/\gamma$, and the characteristic timescale t_c,

$$\mathrm{Oh} = \frac{\mu_2}{\sqrt{\gamma \rho_2 R_j}}, \tag{12}$$

and measures the relative importance of viscous and capillary stresses. The Taylor number measures the relative importance between the electrostatic and capillary stresses,

$$\Gamma = \frac{\varepsilon_o E_{\mathrm{no}}^2 R_j}{\gamma}. \tag{13}$$

$\Gamma = 2$ indicates that the capillary and electrostatic stresses fully balance each other in the baseline jet, i.e., the pressure jump across the jet's surface is zero. Π_t is the ratio between the characteristic timescale and the electrical relaxation time of Fluid 2,

$$\Pi_t = \frac{t_e}{t_c} = \frac{\varepsilon_o/K_2}{\sqrt{\rho_2 R_j^3/\gamma}}. \tag{14}$$

Π_t is indicative of the speed with which the charge in the bulk of Fluid 2 migrates to the surface as the jet deforms. Finally, the Peclet number measures the advection rate to the diffusion rate in the Cahn-Hilliard equation,

$$\mathrm{Pe} = \frac{R_j^3}{\varsigma \gamma t_c}. \tag{15}$$

ς is the mobility parameter which we treat as a constant, such that for all the numerical cases considered in the current study $\varsigma = (R_j \xi)^2/p_c t_c$ [44,45]. Therefore, alternatively we can define $\mathrm{Pe} = 1/\xi^2$.

The problem is axisymmetric and since we consider an infinitely long jet, we apply periodic boundary conditions at $z = 0$ and $z = \lambda$. The boundary conditions for the electrical, hydrodynamic and phase field problems are

$$\boldsymbol{e}_z \cdot \boldsymbol{E}(r, 0, t) = 0, \quad \boldsymbol{e}_z \cdot \boldsymbol{E}(r, \lambda, t) = 0, \quad V(R_e, z, t) = 0, \tag{16}$$

$$\boldsymbol{e}_z \cdot \boldsymbol{u}(r, 0, t) = 0, \quad \boldsymbol{e}_z \cdot \boldsymbol{u}(r, \lambda, t) = 0, \tag{17}$$

$$\frac{\partial[\boldsymbol{e}_r \cdot \boldsymbol{u}(r, 0, t)]}{\partial z} = 0, \quad \frac{\partial[\boldsymbol{e}_r \cdot \boldsymbol{u}(r, \lambda, t)]}{\partial z} = 0, \tag{18}$$

$$\boldsymbol{e}_z \cdot \nabla \phi = 0 \quad \textit{at } z = 0,\ \lambda, \quad \phi(R_e, z, t) = -1. \tag{19}$$

Along the symmetry axis ($r = 0$) the boundary conditions on the velocity vector are:

$$\boldsymbol{e}_r \cdot \boldsymbol{u}(0, z, t) = 0, \quad \frac{\partial[\boldsymbol{e}_z \cdot \boldsymbol{u}(0, z, t)]}{\partial r} = 0. \tag{20}$$

$\boldsymbol{e}_r$ and $\boldsymbol{e}_z$ represent the unit vectors in the radial and the axial directions.

We solve the electrohydrodynamic and phase field equations using the commercial COMSOL Multiphysics software [46]. Initially, a homogeneous volumetric charge $\rho_{\text{eo}} = 2$ in Fluid 2 is allowed to relax to the perturbed interface (2) by only solving the electric problem ($\boldsymbol{u} \equiv 0$). Once the charge is relaxed, the full set of equations is solved yielding the evolution of the jet and eventual breakup into droplets. The time dependent simulations are solved using a parallel sparse direct solver, MUMPS with backward differential formulation (BDF) for running the time stepping. In all simulations we use uniform meshing for the jet with node spacing h, such that $1/h = 33$. The thickness parameter for the phase field model is set such that $\xi = 0.5h$. We have verified that for $\xi = 1/100$ and $\xi = 1/66$, the numerical results are independent of the grid size. The simulations are done at fixed values of Π_t, Pe, and ε_2, and varying the Taylor number, the Ohnesorge number, and the wave number to study the effects of these parameters. We set $\Pi_t = 0.02$ and $\varepsilon_2 = 12.2$, which are the values associated with the ionic liquid EMI-Im and whose cone-jets have been characterized in detail [47]; the small Π_t value is typical of cone-jets of highly conducting liquids, suggesting that under these electrospraying conditions the charge in the bulk rapidly relaxes to the surface and the breakup is quasiequipotential. We set Pe = 4356, which is equivalent to using a thickness parameter $\xi = 1/66$. In the Appendix we validate conservation of charge within the simulation domain while letting the jet deform and break into droplets. The maximum variation is within 1%–1.7% of the total charge.

III. CONNECTION BETWEEN THE BREAKUP MODEL AND CONE-JETS OF HIGHLY CONDUCTING LIQUIDS

The solution of the breakup model is a function of Γ, Oh, and Π_t. To apply the model to electrosprays, it is useful to express these dimensionless numbers in terms of those commonly used in the parametrization of cone-jets, namely, the dimensionless flow rate Π_Q and the electric Reynolds number Re_K:

$$\Pi_Q = \frac{\rho_2 K_2 Q}{\gamma \varepsilon_0}, \tag{21}$$

$$\text{Re}_K = \left(\frac{\rho_2 \varepsilon_o \gamma^2}{\mu_2^3 K_2}\right)^{1/3}. \tag{22}$$

Re_K is a grouping of physical properties, while Π_Q also contains the flow rate Q. Both sets of dimensionless numbers can be related using well-established scaling laws for the electric current I of a cone-jet and the radius of the jet at the breakup [5]

$$I \cong \alpha(\gamma K_2 Q)^{1/2} = \alpha\left(\frac{\varepsilon_0 \gamma^2}{\rho_2}\right)^{1/2} {\Pi_Q}^{1/2}, \tag{23}$$

$$R_J \cong \beta\left(\frac{\rho_2 \varepsilon_o Q^3}{\gamma K_2}\right)^{1/6} = \beta \frac{\mu_2^2}{\rho_2 \gamma} {\text{Re}_K}^2 {\Pi_Q}^{1/2}, \tag{24}$$

and by noting that the dominant mechanism for charge transport in the jet is convection of the surface charge σ, which makes it possible to estimate the electric field normal to the surface of the jet,

$$E_{\text{no}} = \frac{\sigma}{\varepsilon_o} = \frac{R_J I}{2\varepsilon_o Q} \cong \frac{\alpha\beta}{2} \frac{{\rho_2}^{1/2}\gamma}{{\varepsilon_o}^{1/2}\mu_2} {\text{Re}_K}^{-1}. \tag{25}$$

The factors α and β are dimensionless proportionally constants relating the current of a cone-jet with the characteristic current $(\gamma K_2 Q)^{1/2}$, and the radius of the jet at the breakup with the characteristic radius of the cone-to-jet transition region, $(\rho_2 \varepsilon_o Q^3/\gamma K_2)^{1/6}$. They are relatively insensitive to the operational conditions of electrosprays in the cone-jet mode. The factor α is easily computed from experimental data: $\alpha = 2.6$ fits well data for many liquids in a wide range of operational conditions [5], and has been reproduced by numerical models [43]. The factor β is more difficult to obtain, because it requires measuring radii of jets that often are submicrometric. Recently, values for highly conducting liquids have been inferred [47,48] using an experimental technique developed by Gamero-Castaño [49]. For example, $0.27 \leqslant \beta \leqslant 0.31$ in cone-jets of EMI-Im in the current range 230 nA $\leqslant I \leqslant$ 450 nA, at 21 ^{o}C emitter temperature [47]. Equations (12)–(14), (24), and (25) yield the relationship between the two sets of dimensionless numbers:

$$\Gamma \cong \frac{\alpha^2 \beta^3}{4} \Pi_Q^{1/2}, \tag{26}$$

$$\mathrm{Oh} \cong \left(\beta \Pi_Q^{1/2} \mathrm{Re}_K^2\right)^{-1/2}, \tag{27}$$

$$\Pi_t = \left(\beta \Pi_Q^{1/2}\right)^{-3/2}, \tag{28}$$

making it possible to estimate the ranges of Γ, Oh, and Π_t of cone-jets.

IV. RESULTS AND DISCUSSIONS

A. Validation of the phase field method

We validate the phase field model with the numerical results and experiments reported by López-Herrera and Gañán-Calvo [18]. These authors measure the sizes and charges of primary and satellite droplets resulting from imposed axisymmetric perturbations with different wave numbers, $0.5 < k < 0.9$, at moderate and small Taylor and Ohnesorge numbers, $\Gamma \leqslant 0.9$ and $\mathrm{Oh} \leqslant 0.271$, and nearly equipotential conditions ($\Pi_t \sim 3 \times 10^{-5}$). Figure 2 shows the solution of our model and the comparison with Ref. [18], for $\mathrm{Oh} = 0.079$ and $\Gamma = 0.9$. Throughout the remainder of the article we use the following nomenclature for the droplets: primary droplet, PD, refers to the larger droplets formed at $z = 0$ and $z = \lambda$; satellite droplet SD refers to the droplet that would contain the fluid and charge separated from the primary droplets by the initial pinch-off; this section of fluid may split into two or more droplets if there is a second pinch-off, producing a larger satellite droplet centered at $z = \lambda/2$ and referred to as S, and smaller subsatellite droplets of decreasing size referred to as $S1$, $S2$... formed between the PD and the S droplets. Figure 2(a) shows the evolution of the jet for $k = 0.7$, leading to the formation of a satellite droplet in addition to the primary droplet. The shape of the satellite droplet oscillates due to the slow viscous dissipation of its internal flow. Figure 2(b) compares the radii of the primary and satellite droplets. The radius R_d of a droplet is deduced from its volume right after pinch-off. The agreement between our calculations and the experiments and calculations of López-Herrera and Gañán-Calvo [18] is excellent. As the wave number increases the sizes of the primary and satellite droplets decrease monotonically, a trivial trend resulting from the volume of the jet yielding both droplets, $2\pi^2 R_j^2/k$, and the volume of the satellite being a small fraction of it. Figures 2(c) and 2(d) compare the charge of the primary and satellite droplets expressed as a fraction of the Rayleigh limit,

$$Q_{\mathrm{Ray}} = 8\pi \sqrt{\varepsilon_o \gamma R_d^3}. \tag{29}$$

When the charge of a droplet is above the Rayleigh limit, the droplet becomes unstable and fragments into smaller droplets. The primary droplet is charged to a nearly constant fraction of the Rayleigh limit regardless of the wave number, while in the case of the satellite droplet this ratio increases modestly for decreasing wave number. Collins *et al.* [19] also found this trend in their equipotential study.

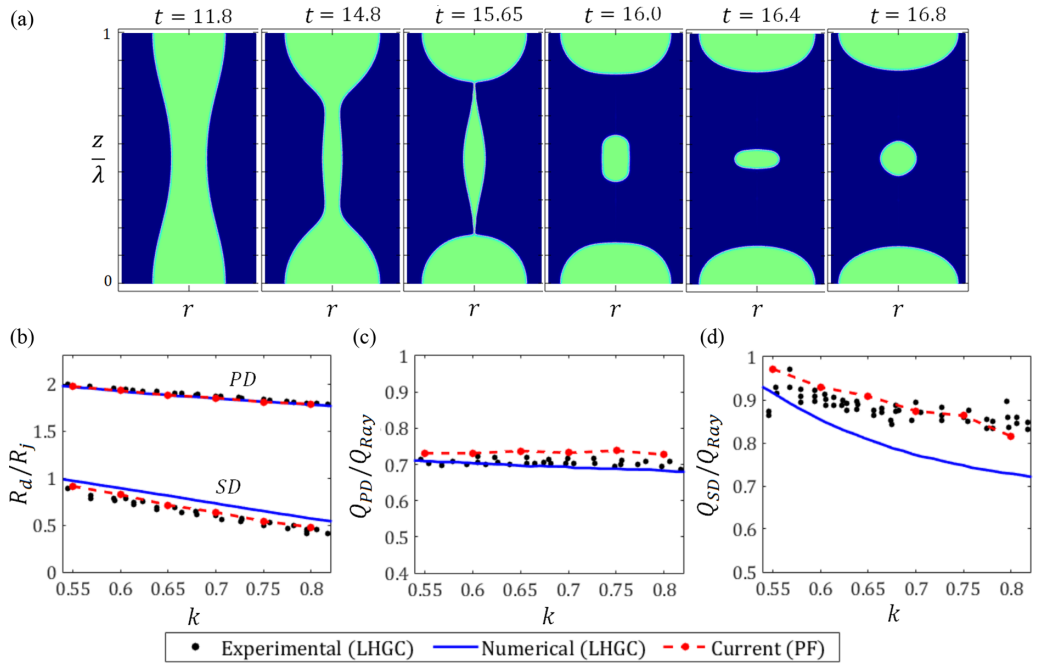

FIG. 2. (a) Evolution of the jet for Oh = 0.079, Γ = 0.9, and $k = 0.7$, the axial axis is normalized by λ; (b) radii of primary and satellite droplets, comparison between the solution of the phase field model (PF) and the experimental and numerical data (LHGC) of López-Herrera and Gañán-Calvo [18] for Oh = 0.079, Γ = 0.9; (c) charge of primary droplets; and (d) charge of satellite droplets. Charges are normalized with the charge of the droplet at the Rayleigh limit.

Figure 3 reproduces the analysis in Fig. 2 under more viscous conditions, Oh = 0.271, and equal electrification level, Γ = 0.9. Figure 3(a) shows that after the initial pinch-off separating the primary droplet and the satellite droplet, the retracting threads connected to the latter undergo a subsequent pinch-off that forms subsatellite droplets. We observe this for all wave numbers considered, $0.55 \leqslant k \leqslant 0.8$. Figure 3(b) compares the radii of PD and SD droplets. There is again excellent agreement between the phase field model and Ref. [18]. Moreover, the size of the SD droplets is slightly smaller than in the less viscous breakup. Figure 3(c) shows that the primary droplets are charged below the Rayleigh limit, although at a slightly higher fraction than for Oh = 0.079; the SD droplets is now slightly smaller and takes less charge from the original jet section. In their experimental study López-Herrera and Gañán-Calvo [18] found that the SD droplets underwent subsequent breakups, however, they did not present the charge carried by them and simply argued that this subsequent breakup was a consequence of their charge levels exceeding the Rayleigh limit. Figure 3(d) shows that the SD droplets are indeed charged above the Rayleigh limit. However, as evident from Fig. 3(a), this section of the jet resulting from the first pinch-off splits into additional droplets before it becomes spherical, with charges and diameters that can be quantified. Figure 3(e) depicts the radius of the satellite droplets S and $S1$ resulting from the second pinch-off, and Fig. 3(f) shows their charge levels. Interestingly, the second pinch-off reduces the charging level of both satellite droplets compared to the original SD droplet, so that the droplets actually forming remain below the Rayleigh limit. In summary, previous studies [18,19] have shown that the charge carried by the SD droplets increases with the Ohnesorge number (at constant Taylor number and wave number); the phase field model reproduces this too, and in addition shows that these SD droplets undergo additional pinch-offs during the jet breakup phase, yielding smaller droplets with charge levels (expressed as a fraction of the Rayleigh limit) smaller than that of the SD parent

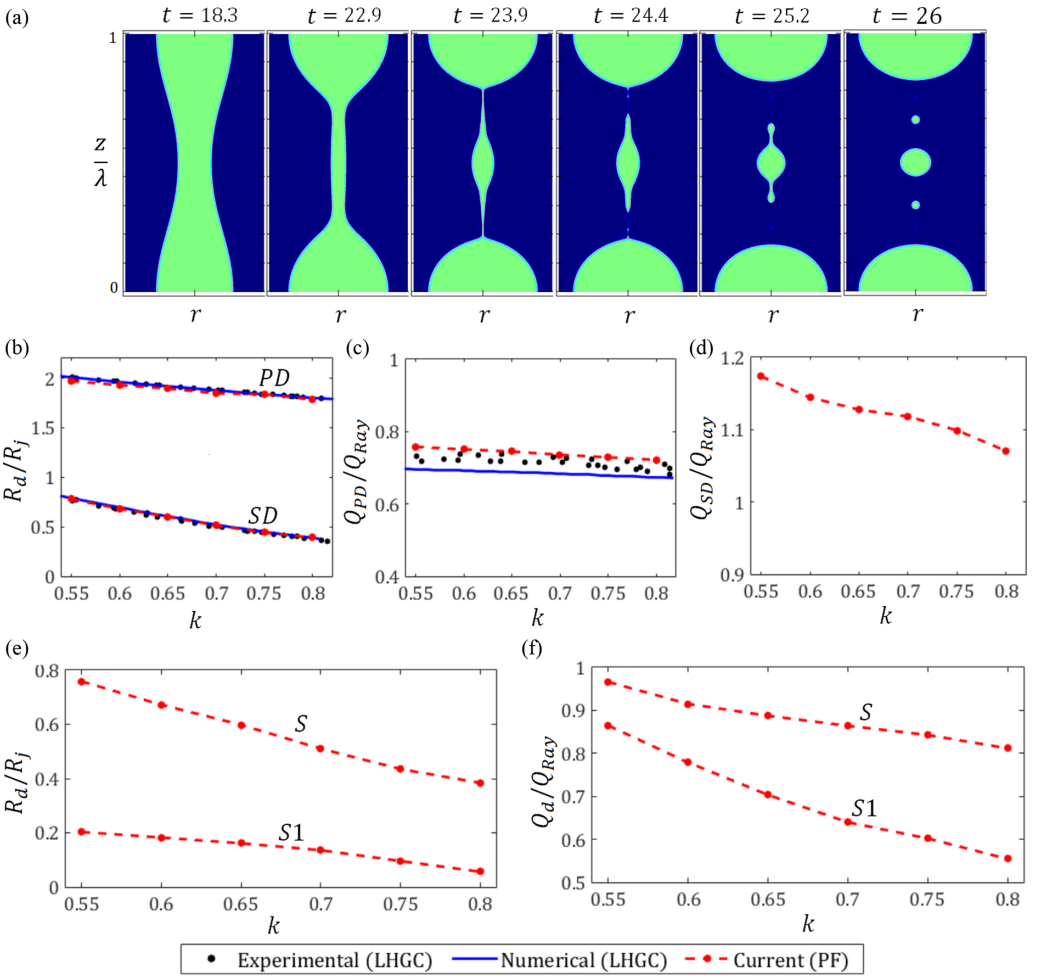

FIG. 3. (a) Evolution of the jet for Oh = 0.271, Γ = 0.9, and $k = 0.7$, the axial axis is normalized by λ; (b) radii of primary and satellite droplets, comparison between the solution of the phase field model (PF) and the experimental and numerical data (LHGC) of López-Herrera and Gañán-Calvo [18] for Oh = 0.271, Γ = 0.9; (c) charge of primary droplets (PD); (d) charge of "satellite droplet" SD; (e) radius of the satellite (S) and subsatellite (S1) droplets; and (f) charge of the satellite (S) and subsatellite (S1) droplets. Charges are normalized with the charge of the droplet at the Rayleigh limit.

droplet. Sections IV B and IV C will show that for higher electrification levels the satellite droplets *S* produced by the second pinch-off may exceed the Rayleigh limit.

B. Jet breakup with low viscous effects

We next study the breakup of jets with reduced viscous effects, Oh = 0.1, at varying levels of electrification and wave numbers, $0 \leqslant \Gamma \leqslant 3$ and $0.5 \leqslant k \leqslant 1$. Figure 4 depicts the evolution of the breakup at representative Taylor numbers and wave numbers. For uncharged jets, Fig. 4(a), the jet initially deforms with the radial velocity being negative at $z = \lambda/2$. This is because in the early stages of the deformation, $z = \lambda/2$ experiences the maximum capillary pressure. The pressure difference between $z = \lambda/2$ and $z = 0$ drives the early deformation of the jet pushing the fluid towards the ends of the jet section. As the deformation proceeds the radial velocity at $z = \lambda/2$

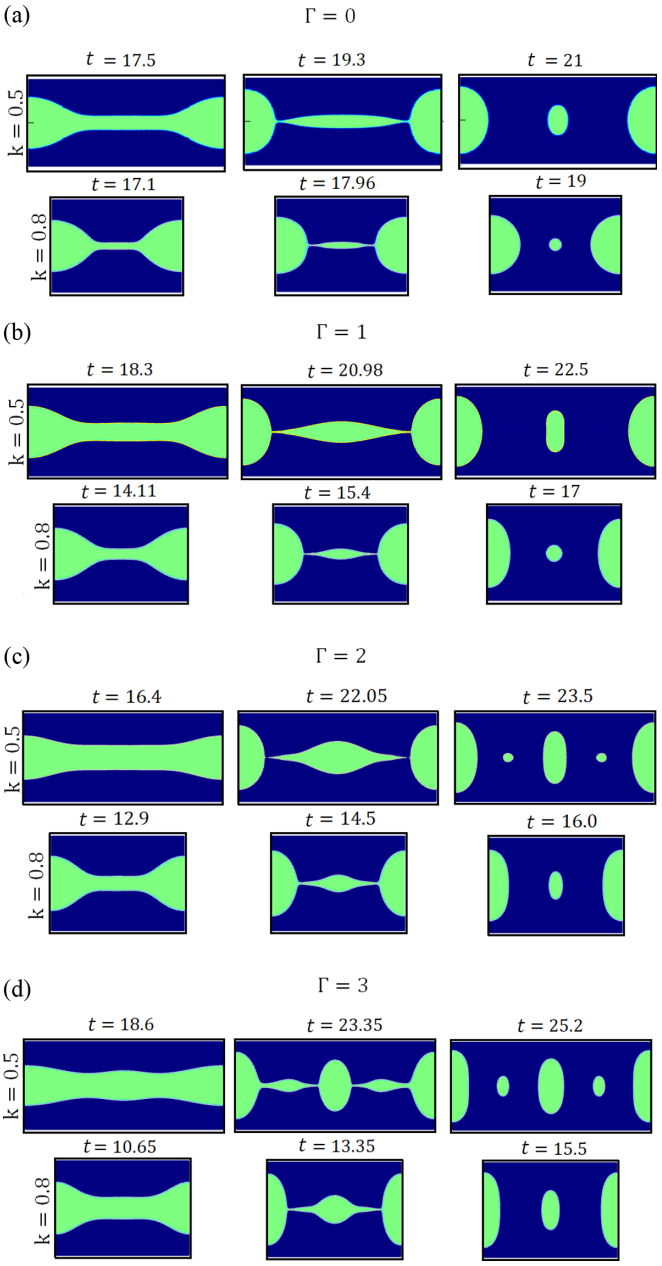

FIG. 4. Evolution of breakups with small viscous effects, Oh = 0.1, for two wave numbers $k = 0.5$ and $k = 0.8$, and several electrification levels: (a) $\Gamma = 0$; (b) $\Gamma = 1$; (c) $\Gamma = 2$; and (d) $\Gamma = 3$.

reverses its direction at $t = 17$ ($k = 0.5$), leading to the formation of a satellite droplet [19,27,33]. Figure 4(b) depicts the deformation and breakup for an electrification level $\Gamma = 1$. In this case the reversal in the sign of the radial velocity of the interface at $z = \lambda/2$ occurs at an earlier stage due to the additional normal electric stresses acting on the interface, which leads to a greater bulge at $z = \lambda/2$. Subsequently, the jet breaks and forms satellite droplets larger than in the uncharged breakup. It is worth noting that for $\Gamma = 0$ and $\Gamma = 1$, only PD and SD droplets are formed for all

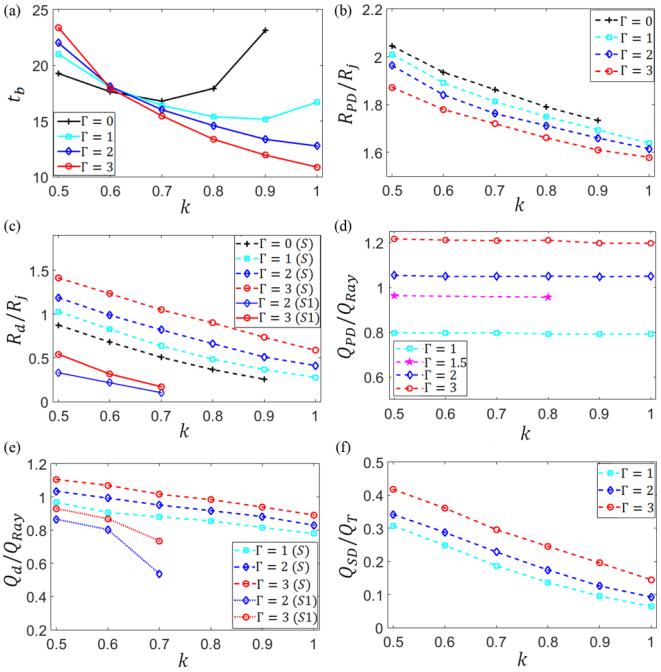

FIG. 5. Results of the phase field model for breakups with small viscous effects, Oh = 0.1, as a function of the Taylor number and wave number: (a) time at first pinch-off; (b) radius of primary droplets; (c) radius of S and $S1$ satellite droplets; (d) charge of the primary droplet relative to its Rayleigh limit; (e) charge of the S and $S1$ satellite droplets relative to their Rayleigh limit; (f) fraction of the total charge carried by the satellite droplets.

the wave numbers studied, i.e., we do not observe subsatellite droplets. Figures 4(c) and 4(d) depict the deformation and breakup of highly charged jets (it is worth restating that the electrostatic stress fully balances the capillary pressure in the nominal jet when $\Gamma = 2$). For $\Gamma = 2$ and $k = 0.5$, the retracting threads formed at the pinch-off undergo an additional breakup leading to the formation of subsatellite droplets. For $\Gamma = 3$ and $k = 0.5$ the radial velocity reversal at $z = \lambda/2$ occurs at a much earlier stage due to the larger electrostatic stresses. The breakup differs in this case in that the first pinch-off actually happens in the thread attached to the S droplet, rather than near the PD droplet. Subsequently and as depicted in the first row in Fig. 4(d), the retracting thread joined to the primary droplet undergoes a second pinch-off leading to the formation of an $S1$ droplet. Therefore, highly charged jets with long wavelengths lead to the formation of subsatellite droplets even at low viscosities.

Figure 5(a) depicts the time at the first pinch-off, which can be regarded as the breakup time. For $0.6 < k < 1$, the breakup time decreases at increasing Taylor number, a trend also observed by Collins *et al.* [19] and Lakdawala *et al.* [27]. Moreover, the wave number with minimum breakup time increases with the Taylor number, i.e., the modal droplet becomes smaller at increasing electrification level. Figures 5(b) and 5(c) show the radius of the primary and satellite droplets. At fixed wave number the radius of the primary droplet decreases at increasing Taylor number because of the earlier reversal in the radial velocity of the interface, which increases the size of the satellite droplet. Subsatellite droplets are not formed at either $\Gamma = 0$ or $\Gamma = 1$, and start to appear at $\Gamma = 2$ and sufficiently long wavelengths. Figure 5(d) depicts the charge carried by the primary droplet as a fraction of the Rayleigh limit. As already observed in Figs. 2 and 3, this ratio is relatively independent of the wave number, and increases with the Taylor number. Primary droplets exceed the Rayleigh limit for $\Gamma \gtrsim 1.5$, an important result for predicting the stability of primary droplets

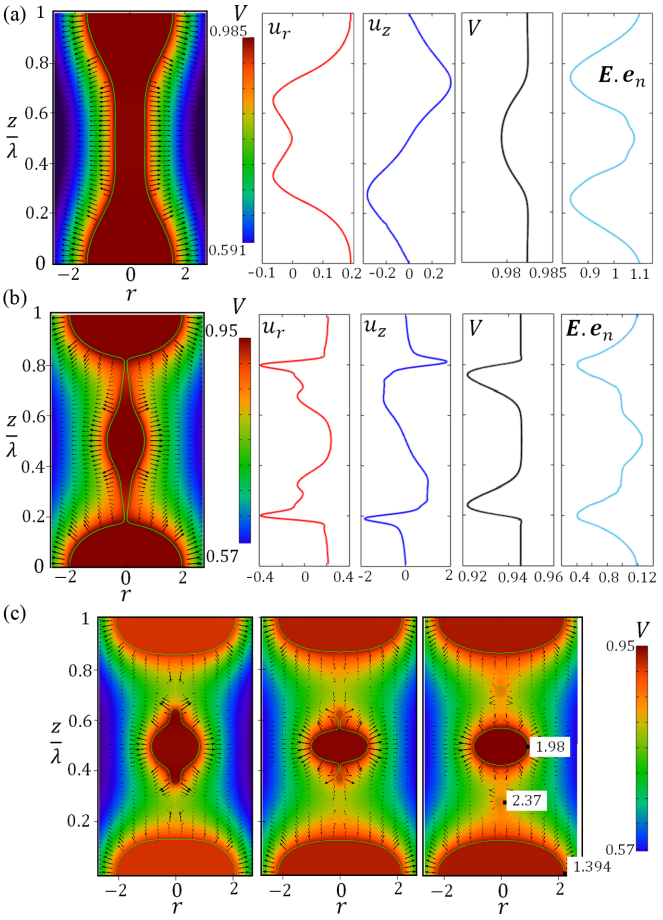

FIG. 6. Electric potential map and radial velocity, axial velocity, potential and normal component of the electric field on the surface, for Oh $= 0.1$, $\Gamma = 2$ and $k = 0.7$: (a) solution at $t = 13.7$ coinciding with zero radial velocity at $z = \lambda/2$; (b) solution just before pinch-off. (c) Electric potential maps before ($t = 16.6$), near ($t = 16.95$), and after ($t = 17.9$) the second pinch-off. The last inset shows the maxima of the electric field.

in low viscous breakups. Figure 5(e) shows the charges carried by the satellite droplets. Although subsatellite droplets are being formed, the S droplets are above the Rayleigh limit for $\Gamma \geqslant 2$ and the longer wavelengths. However, the $S1$ droplets are always charged below the Rayleigh limit. Finally, Fig. 5(f) shows the fraction of the total charge carried by the satellite droplets.

Figure 6(a) shows the electric potential, with arrows representing the direction and strength of the electric field, when the radial velocity of the interface at $z = \lambda/2$ becomes zero before reversing its direction, together with profiles of the radial velocity, axial velocity, potential and normal component of the electric field along the surface. The radial velocity at this time displays minima at $z = 0.35\lambda$ and $z = 0.65\lambda$, which starts creating the curvature for the satellite droplet that will eventually form. The electric potential along the surface is nearly constant, i.e., the jet can be regarded equipotential to a good approximation, as should be expected from the small value of Π_t; furthermore, the potential has very slightly dropped from its initial value of 1 at this point. The electric field on the surface at $z = 0.25\lambda$ and $z = 0.75\lambda$ is partially shielded by the inward bending of the surface, and hence its normal component displays local minima at these points, while there are local maxima at $z = 0, \lambda/2$ and λ. Figure 6(b) depicts the same variables immediately before the first pinch-off. The electric potential along the surface is slightly lower near the pinch-off, a feature

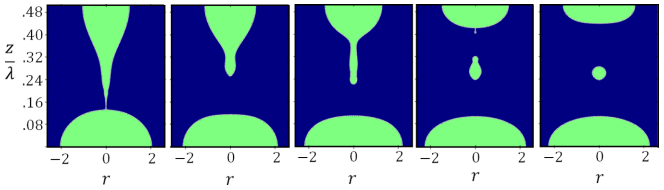

FIG. 7. Retracting thread and subsatellite formation process for $k = 0.5$, $\Gamma = 2$, and $\mathrm{Oh} = 0.1$

also observed by López-Herrera and Gañán-Calvo [18], because the capillary time associated with the local radius of the surface becomes comparable to the electric relaxation time. The radial velocity displays two distinct minima, which later separate the primary and subsatellite $S1$ droplets from the satellite S droplet. Figure 6(c) includes three snapshots with mappings of the electric potential after the first pinch-off, including the formation of a subsatellite droplet. The maximum values of the normalized electric field on the S and $S1$ droplets are 1.98 and 2.37, respectively, and occur at the farthest point from the axis. In particular, the $S1$ droplet features the maximum value of the electric field at any point and time of the calculation.

Figure 7 depicts the evolution of the breakup leading to the formation of a subsatellite droplet ($k = 0.5$, $\Gamma = 2$, $\mathrm{Oh} = 0.1$). A tapered thread connecting the primary droplet and the soon-to-be satellite droplet is severed by the first pinch-off, and retracts towards the SD droplet due to the higher pressure in the tapered end. However, the thread does not fully collapse into the bulk of the liquid, but it starts to elongate backwards toward the primary droplet (see third inset). This thread eventually undergoes a second pinch-off, leading to the formation of the S and $S1$ droplets.

C. Jet breakup with high viscous effects

Figures 8–11 reproduce the same simulations as in Sec. IV B, but for a large Ohnesorge number exemplifying dominant viscous effects, $\mathrm{Oh} = 10$. The geometry of the deforming jet displays several differences with respect to the $\mathrm{Oh} = 0.1$ case. In the absence of electrification, Fig. 8(a), no satellite or subsatellite droplets form. Since inertial effects are negligible, the pressure remains maximum at $z = \lambda/2$ until pinch-off, preventing the formation of satellite droplets [19,50]. Figure 8(b) shows the evolution for a Taylor number of one. In this case satellite and subsatellite droplets form, not driven by inertia but by the electrostatic pressure in the vicinity of $z = \lambda/2$. At the larger Taylor numbers shown in Figs. 8(c) and 8(d), $\Gamma = 2$ and $\Gamma = 3$, three distinct subsatellite droplets are formed along with the primary and satellite droplets for $k = 0.5$, and single subsatellite droplets are formed for the shorter jet section, $k = 0.8$. The mechanism for the formation of the initial SD droplet is different when compared to the $\mathrm{Oh} = 0.1$ case. At small Ohnesorge number the SD droplet is connected to the primary droplets by a tapered thread, whereas at large Ohnesorge number the thread joining the primary and SD droplets is slender and thin. The slender thread coupled with the lack of inertial effects leads to the formation of multiple subsatellite droplets. The breakup behavior is qualitatively similar to that observed in prior studies of highly viscous and uncharged jets (Stoke's limit) surrounded by a fluid of comparable viscosity [21,22,29,30].

The times of the first pinch-off, Fig. 9(a), are over one order of magnitude larger than in Fig. 5(a). t_μ rather than t_c is the appropriate characteristic time for describing the dynamics because inertial effects are negligible, but since we continue using t_c to normalize time the breakup times are much larger than one. Note also that for a given Taylor number, the wave number with minimum breakup time decreases at increasing Onhesorge number. Thus, the wavelength that produces the modal primary droplet increases with the importance of viscous effects, while the intensity of electrification has the opposite effect. The radius of the primary droplets, Fig. 9(b), displays a similar trend as in the low viscosity regime, i.e., the size of the primary droplet decreases as the level of electrification increases due to the larger electric stresses on the interface which leads to the formation of larger

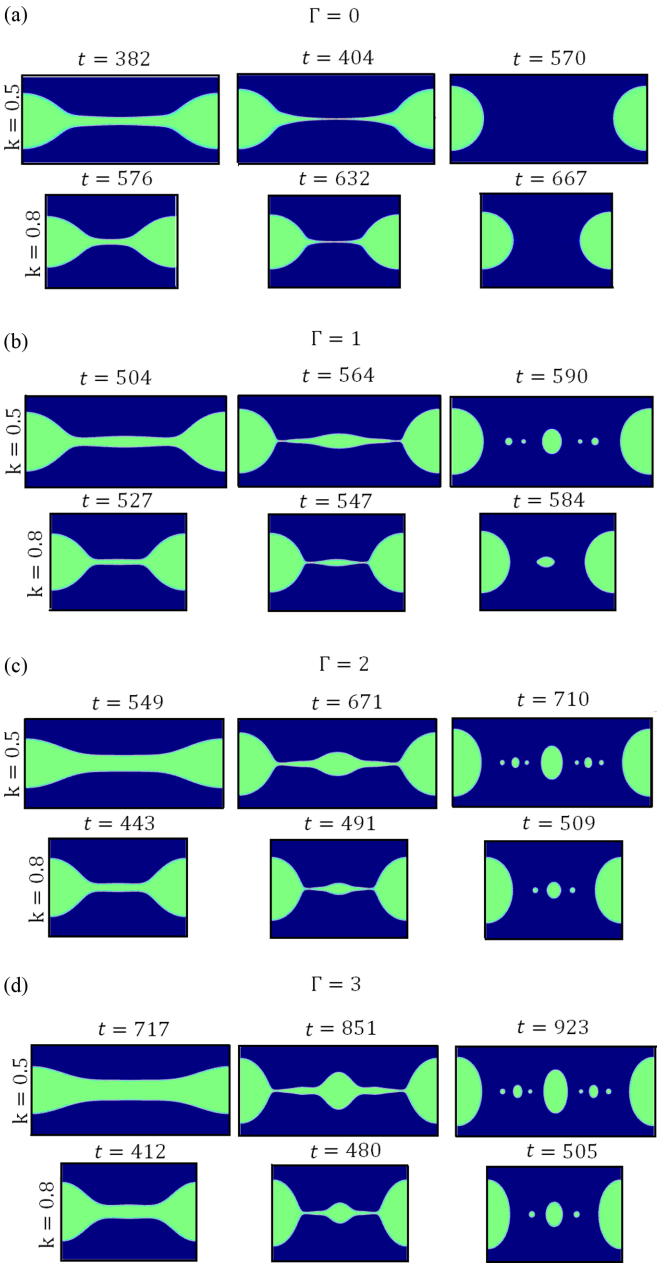

FIG. 8. Evolution of breakups with high viscous effects, Oh = 10, for two wave numbers $k = 0.5$ and $k = 0.8$, and several electrification levels: (a) $\Gamma = 0$; (b) $\Gamma = 1$; (c) $\Gamma = 2$; and (d) $\Gamma = 3$.

satellite droplets. Figure 9(c) depicts the radii of the S and $S1$ droplets (no satellite droplets are formed for $\Gamma = 0$). We only display the radius of $S1$ subsatellite droplet, although two additional subsatellites are formed for $k = 0.5$; for all the other wave numbers only the $S1$ subsatellite droplet forms. The size of the S droplets for a given Γ is smaller in the high viscous regime than in the low viscous regime. This trend could be explained by the fact that in the low viscous case, along with the electric stresses, inertial effects also help in pushing the fluid to the satellite droplet, hence

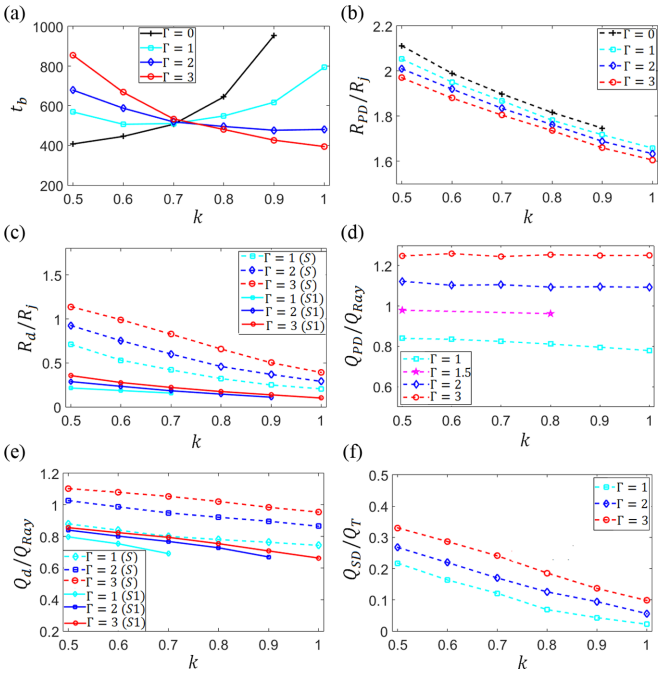

FIG. 9. Results of the phase field model for breakups with high viscous effects, Oh = 10, as a function of the Taylor number and wave number: (a) time at first pinch-off; (b) radius of primary droplets; (c) radius of S and $S1$ satellite droplets; (d) charge of the primary droplet relative to its Rayleigh limit; (e) charge of the S and $S1$ satellite droplets relative to their Rayleigh limit; (f) fraction of the total charge carried by the satellite droplets.

increasing its size. This additional inertial mechanism is not present at Oh $\gg 1$. The trends for the charge of the different droplets relative to the Rayleigh limit, Figs. 9(d) and 9(e), are similar to the low viscosity case. Again, in Fig. 9(d) we include results for $\Gamma = 1.5$ indicating that this value of the Taylor number separates primary droplets that are above ($\Gamma \gtrsim 1.5$) and below ($\Gamma \lesssim 1.5$) the Rayleigh limit, i.e., droplets that are unstable and stable. Interestingly, this stability condition for the primary droplets is largely independent of the wave number and the Onhesorge number. Finally, note that the fraction of the total charge that is carried by satellite droplets is reduced in a breakup dominated by viscous effects [compare Figs. 9(f) and 5(f)].

The surface profiles and electric potential maps in Fig. 10 display similar trends to the Oh = 0.1 case. At any given time, the surface is equipotential to a good approximation. In fact, our definition of Π_t overestimates the time constant for charge relaxation, because t_μ is the correct characteristic time for the evolution of the jet at high Ohnesorge number, and $t_\mu \gg t_c$. The electric field is normal to the surface of the jet, and displays local maxima at the centers of the primary and subsatellite droplets with an absolute maximum on the smallest subsatellite. In Fig. 10(b) for a time close to the first pinch-off we note a distinct feature connected to the formation of subsatellite droplets: in addition to the typical local minima of the radial velocity at $z = 0.2\lambda$ and $z = 0.8\lambda$ leading to the location of the first pinch-off, two additional local minima appear at $z = 0.4\lambda$ and $z = 0.6\lambda$ which lead to the thinning of the retracting thread and eventually to a second pinch-off and subsatellite droplets. Similar features are also observed in the axial velocity profile.

Figure 11 depicts the breakup behavior of the retracting thread for $\Gamma = 2$ and $k = 0.5$. Although the retracting thread moves towards the satellite droplet, the thread is detached from the satellite droplet by a second pinch-off and subsequently undergoes additional pinch-offs to form subsatellite

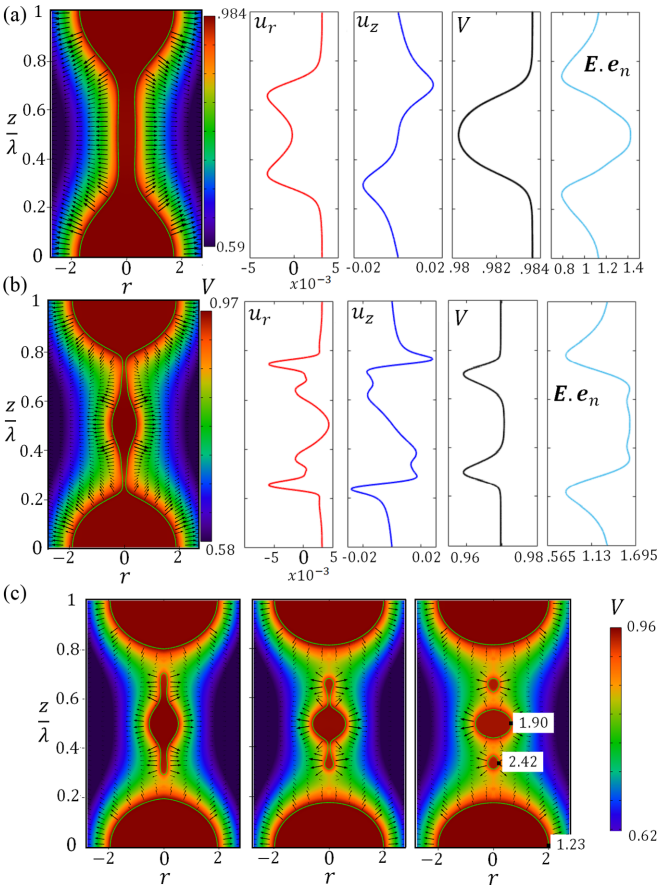

FIG. 10. Electric potential map and radial velocity, axial velocity, potential and normal component of the electric field on the surface, for Oh $= 10$, $\Gamma = 2$ and $k = 0.7$: (a) solution at $t = 453$ coinciding with zero radial velocity at $z = \lambda/2$; and (b) solution just before pinch-off. (c) Electric potential maps before ($t = 538$), at ($t = 554$), and after ($t = 568$) second pinch-off. The last inset shows the location and values of electric field maxima.

droplets. When compared with the breakup in Fig. 10(c) for the same Taylor number and smaller wave number, $k = 0.7$, the behavior is similar but the longer thread produced by the smaller wave number leads to a larger number of subsatellite droplets.

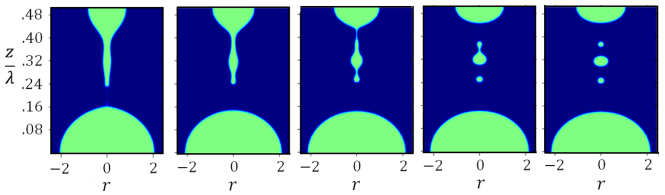

FIG. 11. Formation of subsatellite droplet from the retracting slender thread for Oh $= 10$, $\Gamma = 2$, and $k = 0.5$. $z/\lambda = 0$ depicts the primary droplet location and $z/\lambda = 0.5$ depicts the location of the satellite droplet.

V. CONCLUSIONS

We have developed a leaky-dielectric phase field model to study the deformation and breakup of electrified jets of finite conductivity, performing calculations in wide ranges of the Taylor number, the Ohnesorge number, and the wave number. The phase field method allows us to accurately model the deformation of the jet beyond the first pinch-off and therefore makes it possible to study the formation of subsatellite droplets. However, one of the caveats of the phase field model is the use of a diffuse interface with an artificial finite thickness, and the possibility that some subsatellite droplets may have smaller or comparable diameters. These subsatellite droplets cannot be resolved by the numerical model. These smaller droplets would have size $R_d/R_j \leqslant \xi$, where $\xi = 1/66$. We draw the following main conclusions:

(1) There is an excellent agreement between the solution of the phase field model and the experimental and numerical results of López-Herrera and Gañán-Calvo [18]. The radius of the satellite droplet increases at decreasing Ohnesorge number for fixed Taylor number and wave number. For high Ohnesorge number the satellite droplet SD would be above the Rayleigh limit even at relatively low values of the Taylor number, but it does not form because the retracting liquid threads tend to undergo additional pinch-offs that distribute the charge into subsatellite droplets that are charged below the Rayleigh limit. This phenomenon can only be observed with a phase field model like the one developed in this article.

(2) The Ohnesorge number plays a key role in the size distribution of the droplets. In a highly viscous breakup, the satellite droplet is connected to the primary droplet by a long and slender thread, which undergoes additional pinch-offs to create subsatellite droplets. This feature also exists at low Ohnesorge number and high Taylor number, however and due to the shape of the retracting thread and inertia, fewer subsatellite droplets are produced.

(3) The Taylor number also plays a key role in the size distribution of the droplets. Irrespective of the importance of viscous effects, an increasing level of electrification increases the size of the satellite droplet and hence reduces the radius of the primary droplet. Moreover, the formation of subsatellite droplets is enhanced by increasing electrification levels.

(4) We show that the value 1.5 for the Taylor number separates primary droplets that are above the Rayleigh limit and would be unstable ($\Gamma \gtrsim 1.5$), from primary droplets that are below the Rayleigh limit ($\Gamma \lesssim 1.5$), regardless of the wave number and the Ohnesorge number.

(5) We present formulas for relating the dimensionless numbers parametrizing the phase field model (Γ, Oh, and Π_t) with those parametrizing the state of a cone-jet (Π_Q and Re_K), to apply it to the natural breakup of cone-jets.

ACKNOWLEDGMENTS

K.M. acknowledges Mr. M. Magnani for several useful discussions. This work was partially funded by the Air Force Office of Scientific Research, Award No. FA9550-21-1-0200. K.M. also acknowledges the Science and Engineering Research Board (SERB), DST, India for partial financial support.

APPENDIX: ROLE OF THE OUTER ELECTRODE AND CHARGE CONSERVATION

We test the role of the position of the outer grounded electrode on the dynamics of the deformation and breakup of the electrified jet. For all the simulation results reported in the current article, the outer grounded electrode is located such that $R_e = 12$. Without changing other parameters we run tests by locating the outer electrode such that $R_e = 80$. Figure 12 depicts the profile of the deformation and breakup of the jet for $\mathrm{Oh} = 10$, $\Gamma = 2$ and $k = 0.9$ for the two electrode positions. The profiles of the jet are superimposed on one-another for the same time t. From Fig. 12 we can deduce that the electrode at $R_e = 12$ is sufficiently far for this parameter to have a negligible effect on the solution. Note that the electric field on the surface of the nominal jet does not depend on the position of the electrode, because we are fixing the Taylor number by fixing the volumetric charge

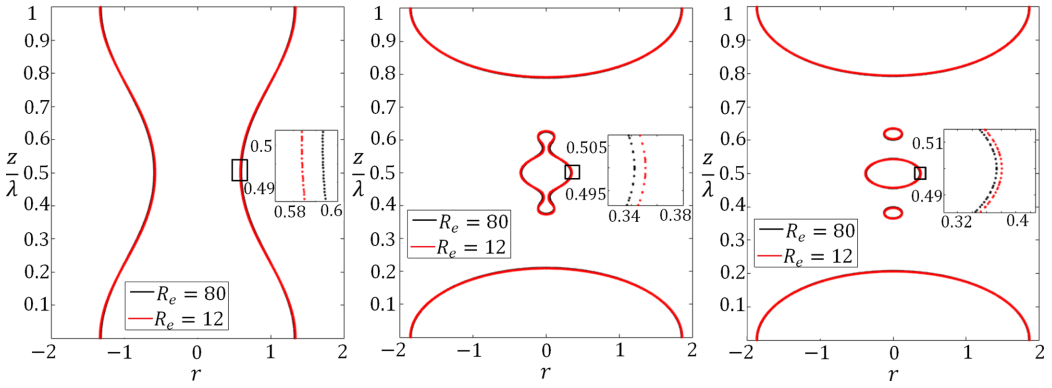

FIG. 12. Comparison between the profile of the interface of the jet for $\Gamma = 2$, Oh $= 10$, and $k = 0.9$ when the grounded electrode is placed far away from the jet ($R_e = 80$) and when $R_e = 12$.

density in the jet. Provided that the outer electrode is sufficiently far away from the jet, the exact position does not have an effect on the dynamics of the breakup.

The initial dimensional volumetric charge in the jet is calculated with the imposed Taylor number. For the surface of a cylinder with surface charge density σ, the dimensional electric field on the surface of the cylinder is given as

$$E(R_j) = \frac{\sigma}{\varepsilon_o}. \tag{A1}$$

Therefore, the dimensional surface charge density is obtained from the Taylor number as

$$\sigma = \sqrt{\frac{\Gamma \varepsilon_o \gamma}{R_j}}. \tag{A2}$$

We subsequently obtain the initial volumetric charge density ρ_{eo} from the surface charge density as $\rho_{\text{eo}} = 2\sigma_e/R_j$. The dimensionless initial volumetric charge density therefore is $\rho_{\text{eo}} = 2$. ρ_{eo} is initially distributed uniformly in the domain $0 < r < 1 + A\cos(kz)$ at $t < 0$. Since the electrical conductivity of the jet (fluid 2) is much higher than the outside passive medium (fluid 1). The charges relax along the mean interface at $t = 0$. At $t = 0$, the electric field variation along the radial direction could be analytically approximated by the expression of electric field variation of a

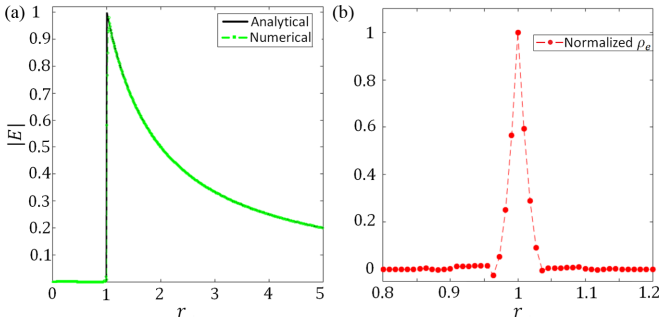

FIG. 13. (a) Electric field variation along the radial direction after the charge relaxation process (at $t = 0$) predicted using the phase-field model and it's comparison with the analytical expression. (b) normalized volumetric charge density along the mean interface at $t = 0$.

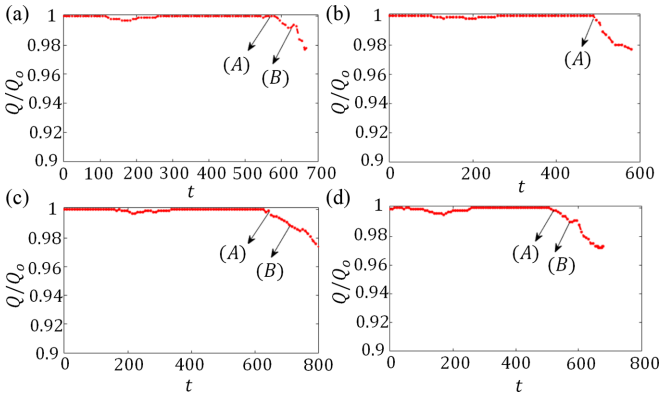

FIG. 14. The total charge in the simulation domain normalized by the initial total charge for different time instants during the deformation-breakup process. (*A*) refers to the time instant when the size and charges of the primary and satellite droplet is made. (*B*) refers to the time instant when the size and charges are measured for subsatellite droplets. (a) $k = 0.6$, $\Gamma = 2$, Oh $= 10$; (b) $k = 1$, $\Gamma = 2$, Oh $= 10$; (c) $k = 0.6$, $\Gamma = 3$, Oh $= 10$; (d) $k = 0.7$, $\Gamma = 3$, Oh $= 10$.

perfectly conducting cylinder, given as

$$\left.\begin{aligned} |\boldsymbol{E}(r<1)| &= 0; \\ |\boldsymbol{E}(r\geqslant 1)| &= \frac{1}{r} \end{aligned}\right\}. \tag{A3}$$

Figure 13(a) depicts the electric field variation along the radial direction predicted using the phase-field model after the charges have relaxed along the mean-interface at $t = 0$ and it's comparison with the analytical expression (32). Since the phase field method is continuous interface method, the electric field in the proximity of $r = 1$ has a continuous and finite slope, however, it compares well with the analytical expression. Figure 13(b) depicts the normalized volumetric charge density.

Since, we apply periodic boundary condition in the domain of the simulation at $z = 0$ and $z = \lambda$, the total charges along one wavelength of the jet should be conserved. Figure 14 depicts the total charge variation in the entire simulation geometry for different cases. Figure 14(a) depicts the total charge variation for Oh $= 10$, $\Gamma = 2$, and $k = 0.6$, the arrows (A) and (B) depict the time instant at which the charges on the droplets are calculated (right after respective pinch-off). After pinch-off there is a loss in the total charge in the geometry. However, since we are only limited to measuring the charges just after each pinch-off process. The charges measured are within a 1–1.7% error range and hence the present setup along with the numerical validation with prior experimental results gives us confidence in our numerical measurements. However, after the formation of primary, satellite and subsatellite droplets we cannot capture the Rayleigh instability process of the droplets which are above the Rayleigh limit, as the charges fail to be conserved in our simulation domain for extended periods after breakup.

[1] J. Zeleny, Instability of electrified liquid surfaces, Phys. Rev. **10**, 1 (1917).

[2] M. Cloupeau and B. Prunet-Foch, Electrostatic spraying of liquids in cone-jet mode, J. Electrost. **22**, 135 (1989).

[3] L. D. Juan and J. F. de la Mora, Charge and size distributions of electrospray drops, J. Colloid Interface Sci. **186**, 280 (1997).

[4] M. Gamero-Castaño and V. Hurby, Electric measurements of charged sprays emitted by cone-jets, J. Fluid Mech. **459**, 245 (2002).

[5] A. Gañán-Calvo, J. López-Herrera, M. Herrada, A. Ramos, and J. Montanero, Review on the physics of electrospray: From electrokinetics to the operating conditions of single and coaxial Taylor cone-jets, and ac electrospray, J. Aerosol Sci. **125**, 32 (2018).
[6] J. Rosell-Llompart, J. Grifoll, and I. Loscertales, Electrosprays in the cone-jet mode: From Taylor cone formation to spray development, J. Aerosol Sci. **125**, 2 (2018).
[7] A. B. Basset, Waves and jets in a viscous liquid, Am. J. Maths **16**, 93 (1894).
[8] J. R. Melcher, Field-coupled surface waves, (MIT Press, 1963).
[9] D. A. Saville, Stability of electrically charged viscous cylinders, Phys. Fluids **14**, 1095 (1971).
[10] A. Yarin, W. Kataphinan, and D. Reneker, Branching in electrospinning of nanofibers, J. Appl. Phys. **98**, 064501 (2005).
[11] A. Mestel, Electrohydrodynamic stability of a slightly viscous jet, J. Fluid Mech. **274**, 93 (1994).
[12] A. Mestel, Electrohydrodynamic stability of a highly viscous jet, J. Fluid Mech. **312**, 311 (1996).
[13] J. M. López-Herrera, R.-C. P., and A. M. Gañán-Calvo, Linear stability analysis of axisymmetric perturbations in imperfectly conducting liquid jets, Phys. Fluids. **17**, 034106 (2005).
[14] Q. Wang, Breakup of a poorly conducting liquid thread subject to a radial electric field at zero Reynolds number, Phys. Fluids **24**, 102102 (2012).
[15] E. R. Setiawan and S. D. Heister, Nonlinear modeling of an infinite electrified jet, J. Electrost. **42**, 243 (1997).
[16] J. M. López-Herrera, A. M. Gañán-Calvo, and M. Perez-Saborid, One-dimensional simulation of the breakup of capillary jets of conducting liquids: Application to EHD spraying, J. Aerosol Sci. **30**, 895 (1999).
[17] H. Lee, Drop formation in liquid jets, IBM J. Res. Develop. **18**, 364 (1974).
[18] J. M. López-Herrera and A. M. Gañán-Calvo, A note on charged capillary jet breakup of conducting liquids: Experimental validation of a viscous one-dimensional model, J. Fluid Mech. **501**, 303 (1999).
[19] R. T. Collins, M. T. Harris, and O. A. Basaran, Breakup of electrified jets, J. Fluid Mech. **588**, 75 (2007).
[20] L. Rayleigh, On the equilibrium of liquid conducting masses charged with electricity, Phil. Mag. **14**, 184 (1882).
[21] J. R. Lister and H. A. Stone, Capillary breakup of a viscous thread surrounded by another viscous fluid, Phys. Fluids **10**, 2758 (1998).
[22] R. V. Craster, O. Matar, and D. T. Papageorgiou, On compound threads with large viscosity contrast, J. Fluid Mech. **533**, 95 (2005).
[23] Q. Wang and D. Papageorgiou, Dynamics of a viscous thread surrounded by another viscous fluid in a cylindrical tube under the action of radial electric fields: Breakup and touchdown singularities, J. Fluid Mech. **683**, 27 (2011).
[24] Q. Nie, F. Li, Q. Ma, H. Fang, and Z. Yin, Effects of charge relaxation on the electrohydrodynamic breakup of leaky-dielectric jets, J. Fluid Mech. **925**, A4 (2021).
[25] F. Li, X. Yin, and X. Yin, Small-amplitude shape oscillation and linear instability of an electrically charged viscoelastic liquid droplet, J. Non-Newtonian Fluid Mech. **264**, 85 (2019).
[26] C. Eck, M. Fontelos, G. Grün, F. Klingbeil, and O. Vantzos, On a phase-field model for electrowetting, Interfaces Free Bound **11**, 259 (2009).
[27] A. M. Lakdawala, A. Sharma, and R. Thaokar, A dual grid level set method based study on similarity and difference bewteen interface dynamics for surface tension and radial electric field induced jet breakup, Chem. Eng. Sci. **148**, 238 (2016).
[28] J. M. López-Herrera, A. M. Gañán-Calvo, S. Popinet, and M. A. Herrada, Electrokinetic effects in the breakup of electrified jets: A volume-of-fluid numerical study, Int. J. Multiphase Flow **71**, 14 (2015).
[29] M. Tjahjadi, H. A. Stone, and J. M. Ottino, Satellite and subsatellite formation in capillary breakup: Nonlinear modeling of an infinite electrified jet, J. Fluid Mech. **243**, 297 (1992).
[30] C. F. Brasz, A. Berny, and J. C. Bird, Threshold for discretely self-similar satellite drop formation from a retracting liquid cone, Phys. Rev. Fluids **3**, 104002 (2018).
[31] A. M. Gañán-Calvo, Cone-Jet Analytical Extension of Taylor's Electrostatic Solution and the Asymptotic Universal Scaling Laws in Electrospraying, Phys. Rev. Lett. **79**, 217 (1997).
[32] A. M. Gañán-Calvo, On the general scaling theory for electrospraying, J. Fluid Mech. **507**, 203 (1999).

[33] J. Eggers and E. Villermaux, Physics of liquid jets, Rep. Prog. Phys. **71**, 036601 (2008).
[34] J. M. López-Herrera, A. Gañán-Calvo, and M. Herrada, Absolute to convective instability transition in charged liquid jets, Phys. Fluids **22**, 062002 (2010).
[35] D. M. Anderson, G. B. McFadden and A. A. Wheeler, Diffuse-interface methods in fluid mechanics, Annu. Rev. Fluid Mech. **30**, 139 (1998).
[36] D. Jacqmin, Calculation of two-phase navier-stokes flows using phase-field modelling, J. Comput. Phys. **155**, 96 (1999).
[37] P. Yue, J. Feng, C. Liu, and J. Shen, A diffuse-interface method for simulating two-phase flows of complex fluids, J. Fluid Mech. **515**, 293 (1999).
[38] J. M. López-Herrera, S. Popinet, and M. A. Herrada, A charge-conservative approach for simulating electrohydrodynamic two-phase flows using volume-of-fluid, J. Comput. Phys. **230**, 1939 (2011).
[39] G. Tomar, D. Gerlach, G. Biswas, N. Alleborn, A. Sharma, F. Durst, S. Welch, and A. Delgado, Two-phase electrohydrodynamic simulations using a volume-of-fluid approach, J. Comput. Phys. **227**, 1267 (2007).
[40] I. Roghair, M. Musterd, D. Ende, C. Kleijin, M. Kruetzer, and F. Mugele, A numerical technique to simulate display pixels based on electrowetting, Microfluidics and Nanofluidics **19**, 465 (2015).
[41] L. Landau, J. Bell, M. Kearsley, L. Pitaevskii, E. Lifshitz, and J. Sykes, Electrodynamics of continuous media, Vol. 8 (Elsevier, 2013).
[42] D. Saville, Electrohydrodynamics: The Taylor-Melcher leaky dielectric model, Annu. Rev. Fluid Mech. **29**, 27 (1997).
[43] M. Gamero-Castaño and M. Magnani, Numerical simulation of electrospraying in the cone-jet mode, J. Fluid Mech. **859**, 247 (2019).
[44] S. Mandal, U. Ghosh, A. Bandopadhyay, and S. Chakraborty, Electro-osmosis of superimposed fluids in the presence of modulated charged surfaces in narrow confinements, J. Fluid Mech. **776**, 390 (2015).
[45] H. Ding, M. Gilani, and P. Spelt, Sliding, pinch-off and detachment of a droplet on a wall in shear flow, J. Fluid Mech. **664** (2010).
[46] I. Comsol, Comsol, Inc. Comsol multiphysics reference manual, COMSOL (2019).
[47] M. Gamero-Castaño and A. Cisquella-Serra, Electrosprays of highly conducting liquids: A study of droplet and ion emission based on retarding potential and time-of-flight spectrometry, Phys. Rev. Fluids **6**, 013701 (2020).
[48] S. Miller, J. Ulibarri-Sanchez, B. Prince, and R. Bemish, Capillary ionic liquid electrospray: beam compositional analysis by orthogonal time-of-flight mass spectrometry, J. Fluid Mech. **928**, A12 (2021).
[49] M. Gamero-Castaño, The structure of electrospray beams in vacuum, J. Fluid Mech. **604**, 339 (2008).
[50] D. T. Papageorgiou, On the breakup of viscous-liquid threads, Phys. Fluids **7**, 1529 (1995).